ADVANCED FUNCTIONAL MATERIALS
www.afm-journal.de

Materials Views
www.MaterialsViews.com

In Situ Formation of Conductive Metal Sulfide Domain in Metal Oxide Matrix: An Efficient Way to Improve the Electrochemical Activity of Semiconducting Metal Oxide

*In Young Kim, Jiyoon Seo, Seung Mi Oh, Sharad B. Patil, and Seong-Ju Hwang**

A new effective way to improve the electrochemical activity of semiconducting metal oxide is developed by the in situ formation of conductive metal sulfide domain in the metal oxide matrix. The $Li_{0.96}Ti_{1.08}S_2$–$Li_4Ti_5O_{12}$ nanocomposites with tunable compositions and electrical properties are synthesized by the reaction of $Li_4Ti_5O_{12}$ with CS_2 at elevated temperature. The resulting incorporation of conductive $Li_{0.96}Ti_{1.08}S_2$ domain in the $Li_4Ti_5O_{12}$ matrix is effective in enhancing the electrical conductivity and electrode activity of semiconducting lithium titanate. As anode materials for lithium ion batteries, the obtained $Li_{0.96}Ti_{1.08}S_2$–$Li_4Ti_5O_{12}$ nanocomposites show much greater discharge capacity and better rate characteristics than does the pristine $Li_4Ti_5O_{12}$. The usefulness of the present method is further evidenced from the improvement of the electrochemical activity of semiconducting $CsTi_2NbO_7$ after the reaction with CS_2. The present study clearly demonstrates the in situ formation of conductive metal sulfide domain using CS_2 liquid can provide an efficient and universal way to improve the electrode functionality of semiconducting metal oxide.

1. Introduction

Lithium ion batteries (LIBs) receive prime attention as one of the most promising power sources for electric vehicle (EV) because of their long cycle life, high energy density, high work potential, and good rate capability.[1] Even though carbon-based anode materials used in commercialized LIBs boast many advantages such as low price, rich abundance, and low toxicity, their low working potential approaching to 0 V at the end of lithiation process causes serious safety problems originating from the decomposition of electrolyte and the dendritic growth of Li metal on the surface of anode material.[1,2] As an alternative anode material, spinel-structured $Li_4Ti_5O_{12}$ attracts a great deal of research activity because of its highly stable operation potential of 1.55 V versus Li/Li^+ and its excellent cyclability originating from negligible volume change during repeated Li^+ insertion–extraction process.[3] The remarkable safety and reliability of the lithium titanate render this material one of the most suitable anode materials for the EV application. However, the rate performance of lithium titanate is seriously limited by its low electronic and ionic conductivities. Such poor charge transport characteristic of $Li_4Ti_5O_{12}$ basically results from its wide bandgap energy related to the empty 3d states of Ti^{4+} ions.[3f,k] Various attempts such as cationic and anionic doping, and the hybridization and surface coating with conductive carbon are made to circumvent this drawback of lithium titanate.[3] Although these strategies are somewhat successful in improving the electrode activity of metal oxide, they might cause other several side effects such as the lowering of thermal stability. In general, the metal sulfide possesses smaller bandgap energy and higher electrical conductivity than does the corresponding metal oxide, since (metal–sulfur) bond is more covalent than (metal–oxygen) bond.[4] The composite formation with conductive metal sulfide can provide new efficient way to improve the electrode performance of semiconducting metal oxide through the increase of electrical conductivity. However, the formation of metal sulfide domain in the pristine metal oxide domain cannot be achieved by the use of conventional sulfurization agent such as thiourea, ammonium sulfide, sodium sulfide, and elemental sulfur due to their limited diffusivity into the solid lattice. Instead of the formation of metal sulfide domain, this process leads to the formation of sulfate (SO_4^{2-}) species on the surface of metal oxide.[5] The effective formation of metal sulfide grains in the solid lattice might be achieved by the use of gaseous agents such as H_2S. However, the high toxicity of hydrogen sulfide might cause serious safety problems.[6] Instead, less toxic CS_2 liquid with Ar carrier gas can be used as a sulfurization agent to provide a safe and scalable synthetic method for metal oxide–metal sulfide nanocomposites. To the best of our knowledge, there is no report about the in situ incorporation of conductive metal sulfide domain to improve the electrochemical activity of semiconducting metal oxides.

In the present study, a novel effective way to improve the electrode activity of semiconducting metal oxide is developed on the basis of the in situ formation of conductive metal sulfide ($Li_xTi_yS_2$) domain in the metal oxide ($Li_4Ti_5O_{12}$) matrix using the CS_2 liquid. The experimental setup for this experiment is illustrated

Dr. I. Y. Kim, J. Seo, S. M. Oh, Dr. S. B. Patil
Prof. S.-J. Hwang
Department of Chemistry and Nanoscience
College of Natural Sciences
Ewha Womans University
Seoul 120-750, Korea
E-mail: hwangsju@ewha.ac.kr

DOI: 10.1002/adfm.201501478

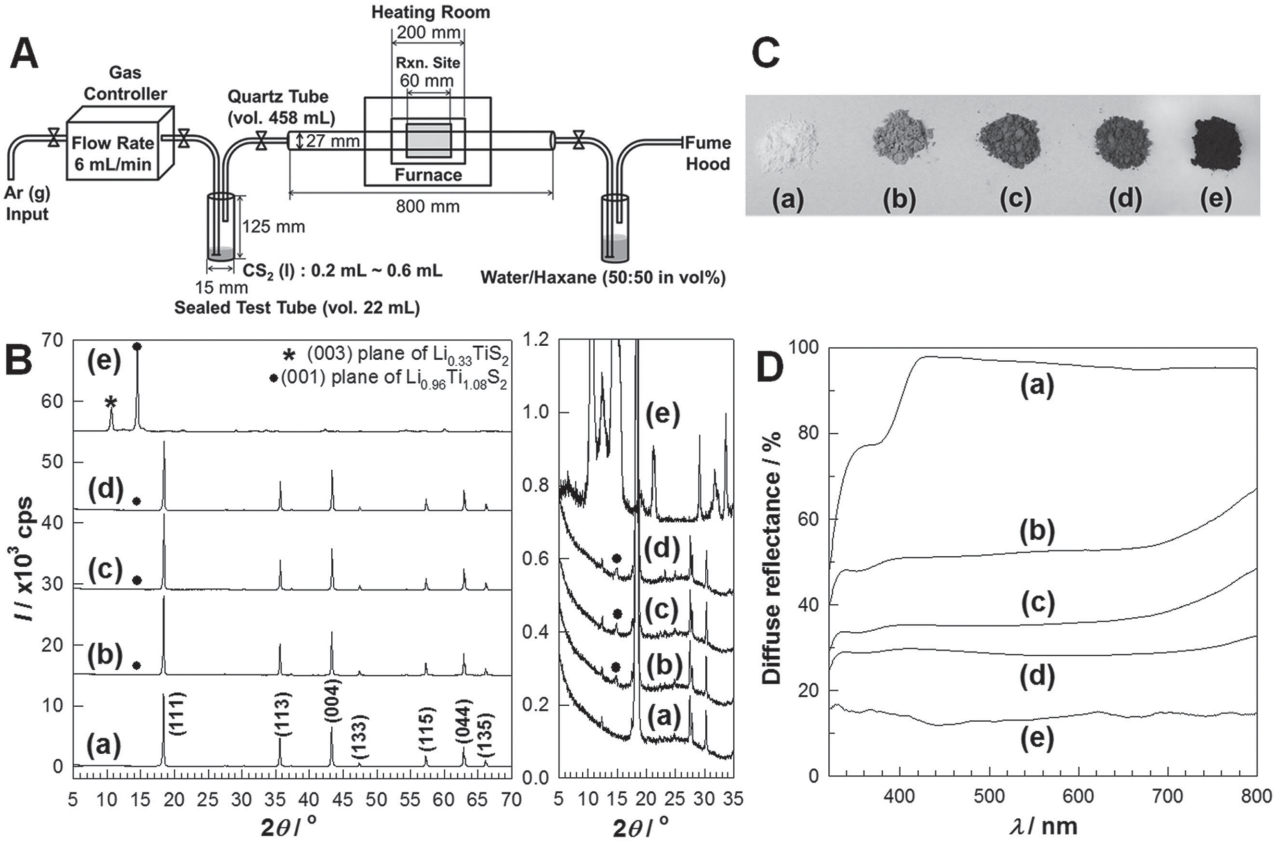

Figure 1. A) Schematic diagram of experimental setup for the in situ formation of metal sulfide domains in semiconducting metal oxide matrix. B) Powder XRD patterns and their expanded view for low region ($2\theta = 5°–35°$), C) photoimages, and D) diffuse reflectance UV–vis spectra of a) the pristine $Li_4Ti_5O_{12}$, the $Li_{0.96}Ti_{1.08}S_2$–$Li_4Ti_5O_{12}$ composites of b) **SLTO1**, c) **SLTO2**, and d) **SLTO3**, and e) the reference $Li_xTi_yS_2$.

in **Figure 1**A. The crystal structures, composite structures, and chemical bonding natures of the obtained $Li_xTi_yS_2$–$Li_4Ti_5O_{12}$ nanocomposites are systematically investigated to understand the effect of composite formation with metal sulfide on the physicochemical properties of lithium titanate. The $Li_xTi_yS_2$–$Li_4Ti_5O_{12}$ nanocomposites are tested as anode materials for LIBs to probe the usefulness of the present method as a tool to enhance the electrode performance of metal oxide-based materials. To study the effect of metal sulfide content on the physicochemical properties and electrode activities of the $Li_xTi_yS_2$–$Li_4Ti_5O_{12}$ nanocomposite, several volumes of liquid CS_2 (0.2, 0.4, and 0.6 mL) are applied for 1 g of the pristine $Li_4Ti_5O_{12}$ material. Hereafter the resulting $Li_xTi_yS_2$–$Li_4Ti_5O_{12}$ nanocomposites are denoted as **SLTO1**, **SLTO2**, and **SLTO3**, respectively. As a reference, conductive $Li_xTi_yS_2$ material is also prepared by the chemical Li intercalation of TiS_2. Additionally the present sulfurization method is applied for the other semiconducting metal oxide of $CsTi_2NbO_7$ to verify the universal applicability of this method.

2. Results and Discussion

2.1. Powder X-Ray Diffraction (XRD) and Elemental Analyses

The crystal structures of the $Li_xTi_yS_2$–$Li_4Ti_5O_{12}$ nanocomposites are examined with powder XRD analysis. As shown in Figure 1B, the pristine $Li_4Ti_5O_{12}$ shows well-developed XRD pattern of cubic spinel structure with the lattice parameter of $a \approx 8.36$ Å. The reference $Li_xTi_yS_2$ displays Bragg reflections of two kinds of intercalated phases of $Li_{0.33}TiS_2$ and $Li_{0.96}Ti_{1.08}S_2$ with different lithium contents (PDF#37-0939 and PDF#40-1093, respectively), which is ascribable to the nonuniform distribution of intercalated Li^+ ions in the interlayer of TiS_2.[7] The $Li_xTi_yS_2$–$Li_4Ti_5O_{12}$ nanocomposites exhibit the XRD peaks corresponding to cubic spinel $Li_4Ti_5O_{12}$ and $Li_{0.96}Ti_{1.08}S_2$ phases, indicating the formation of mixed metal oxide–metal sulfide nanocomposite. The $Li_{0.96}Ti_{1.08}S_2$-related XRD peaks become stronger with increasing the amount of CS_2 liquid used. According to the least squares-fitting analysis, the lattice parameter of the $Li_4Ti_5O_{12}$ component in the present nanocomposites is determined to be $a \approx 8.36$, ≈8.35, and ≈8.35 Å for **SLTO1**, **SLTO2**, and **SLTO3**, respectively, indicating the negligible variation of lattice parameter upon the reaction with CS_2. Taking into account much larger size of sulfur than oxygen,[8] the observed little change of lattice volume strongly suggests no replacement of oxygen with sulfur in the cubic spinel $Li_4Ti_5O_{12}$ lattice. The present XRD results clearly demonstrate that the calcination in CS_2 flow is quite effective in forming mixed metal sulfide–metal oxide nanocomposites rather than sulfur-substituted metal oxide.

The chemical compositions of the present nanocomposite materials are determined with the elemental (CHNS) analysis. The sulfur contents of the $Li_{0.96}Ti_{1.08}S_2$–$Li_4Ti_5O_{12}$ nanocomposites

are estimated to be 0.40, 0.67, and 1.76 wt% for **SLTO1**, **SLTO2**, and **SLTO3**, respectively. On the basis of this result, the compositions of the $Li_{0.96}Ti_{1.08}S_2$–$Li_4Ti_5O_{12}$ nanocomposites are determined as $0.03Li_{0.96}Ti_{1.08}S_2$–$Li_4Ti_5O_{12}$, $0.05Li_{0.96}Ti_{1.08}S_2$–$Li_4Ti_5O_{12}$, and $0.13Li_{0.96}Ti_{1.08}S_2$–$Li_4Ti_5O_{12}$ for **SLTO1**, **SLTO2**, and **SLTO3**, respectively, confirming the gradual increase of the $Li_{0.96}Ti_{1.08}S_2$ content, as plotted in the Figure S1 (Supporting Information).

2.2. Photoimage and Diffuse Reflectance UV–Vis Spectroscopy

As illustrated in Figure 1C, the reaction of the pristine $Li_4Ti_5O_{12}$ with CS_2 leads to a distinct color change from white to dark grey, strongly suggesting the enhanced absorption of visible light and the increase of electrical conductivity. As the amount of CS_2 used increases, the color of the resulting nanocomposites becomes darker, indicating the effective control of the optical property and composition of the $Li_{0.96}Ti_{1.08}S_2$–$Li_4Ti_5O_{12}$ nanocomposite via the change of the amount of CS_2 reactant. The evolutions of the optical properties and electronic structures of the $Li_{0.96}Ti_{1.08}S_2$–$Li_4Ti_5O_{12}$ nanocomposites are examined with diffuse reflectance UV–vis spectroscopy. As presented in Figure 1D, the pristine $Li_4Ti_5O_{12}$ material displays a distinct absorption edge at around 355 nm, indicating its semiconducting nature with the bandgap energy of 3.5 eV. Conversely, no absorption edge is discernible for the reference $Li_xTi_yS_2$, clearly demonstrating the metallic nature of this metal sulfide. A close inspection reveals that the composite formation does not induce a notable change in the position of absorption edge, indicating the negligible change of the bandgap energy of lithium titanate upon the reaction with CS_2. This is in good agreement with no significant variation of the lattice parameter of $Li_4Ti_5O_{12}$ component upon the composite formation with $Li_xTi_yS_2$. As the amount of CS_2 reactant increases, the visible light absorption of the $Li_{0.96}Ti_{1.08}S_2$–$Li_4Ti_5O_{12}$ nanocomposites becomes stronger, confirming the increase of the content of metallic metal sulfide phase. This observation is in good agreement with the color change of the present materials depending on the $Li_{0.96}Ti_{1.08}S_2$ content.

2.3. Field Emission-Scanning Electron Microscopy (FE-SEM) and N_2 Adsorption–Desorption Isotherm Analyses

The crystal morphologies of the present nanocomposites are probed with FE-SEM, see Figure S2 (Supporting Information). The pristine $Li_4Ti_5O_{12}$ material shows irregular polyhedral crystal shape with the average size of ≈1 μm. All of the present nanocomposites of the **SLTO1**, **SLTO2**, and **SLTO3** retain the original crystal morphology of the pristine $Li_4Ti_5O_{12}$ without the formation of any secondary structure, indicating no significant change of crystal shape upon the reaction with CS_2. This observation highlights the effective composite formation between $Li_{0.96}Ti_{1.08}S_2$ and $Li_4Ti_5O_{12}$ domains upon the reaction with CS_2 instead of surface coating.

The surface areas and porosities of the pristine $Li_4Ti_5O_{12}$ and the $Li_{0.96}Ti_{1.08}S_2$–$Li_4Ti_5O_{12}$ nanocomposites are investigated with N_2 adsorption–desorption isotherm measurements, see Figure S3 (Supporting Information). Regardless of the $Li_{0.96}Ti_{1.08}S_2$ content, all the present $Li_{0.96}Ti_{1.08}S_2$–$Li_4Ti_5O_{12}$ nanocomposites possess the same surface area of ≈2–3 $m^2\ g^{-1}$, which is almost identical to the surface area of the pristine $Li_4Ti_5O_{12}$ (≈3 $m^2\ g^{-1}$). This clearly demonstrates negligible influence of the composite formation on the surface area and surface structure of the pristine lithium titanate.

2.4. Micro-Raman Spectroscopic and Transmission Electron Microscopy (TEM) Analyses

The chemical bonding natures of the $Li_{0.96}Ti_{1.08}S_2$–$Li_4Ti_5O_{12}$ nanocomposites are studied with micro-Raman spectroscopy. As plotted in **Figure 2**A, the pristine $Li_4Ti_5O_{12}$ material exhibits typical Raman signals of cubic spinel lithium titanate at 99, 235, 430, and 675 cm^{-1} whereas two intense Raman features appear at 225 and 335 cm^{-1} for the $Li_xTi_yS_2$ reference.[9] The low content of $Li_{0.96}Ti_{1.08}S_2$ phase in the **SLTO1** and **SLTO2** nanocomposites prevents from clearly observing the Raman signals of this minor phase. However, the **SLTO3** material with higher $Li_{0.96}Ti_{1.08}S_2$ content exhibits a distinct Raman feature at 335 cm^{-1} corresponding to A_{1g} mode of the $Li_{0.96}Ti_{1.08}S_2$ phase, underscoring the successful incorporation of metal sulfide domain into the lithium titanate matrix. The spatial distribution of $Li_{0.96}Ti_{1.08}S_2$ domain in the matrix of **SLTO3** nanocomposite is investigated by illustrating the spatial variation of the relative ratio of two main peaks of both $Li_{0.96}Ti_{1.08}S_2$ and $Li_4Ti_5O_{12}$ phases at 335 and 235 cm^{-1}, i.e., I_{335}/I_{235}. As can be seen clearly from Figure 2B, the $Li_{0.96}Ti_{1.08}S_2$ domains are embedded in the host $Li_4Ti_5O_{12}$ matrix. This can be regarded as strong evidence for the successful in situ formation of $Li_{0.96}Ti_{1.08}S_2$ domains in the $Li_4Ti_5O_{12}$ matrix by the reaction with CS_2. It is noteworthy that all the $Li_{0.96}Ti_{1.08}S_2$–$Li_4Ti_5O_{12}$ nanocomposites do not display any carbon-related Raman features at 1200–1600 cm^{-1}, indicating the absence of carbon species in these materials. This finding confirms that the color change and enhanced electrical conductivity of $Li_4Ti_5O_{12}$ after the reaction with CS_2 are attributable to the formation of conductive $Li_{0.96}Ti_{1.08}S_2$, not to the incorporation of carbon species.

The formation of $Li_{0.96}Ti_{1.08}S_2$ domains in the $Li_4Ti_5O_{12}$ matrix is further evidenced by TEM analysis for the **SLTO3** material having the highest sulfide content. As illustrated in Figure 2C, the present **SLTO3** material shows typical hexagonal selected area electron diffraction (SAED) pattern corresponding to the {044} planes of cubic spinel $Li_4Ti_5O_{12}$ structure. The incorporation of $Li_{0.96}Ti_{1.08}S_2$ domain is obviously confirmed by the observation of the lattice fringe of (001) plane from the high resolution-transmission electron microscopy (HR-TEM) image in Figure 2D. Also the elemental maps from the scanning transmission electron microscopy-high angle annular dark field (STEM-HAADF) image clearly illustrate the uniform distribution of sulfur, titanium, and oxygen for the present **SLTO3** nanocomposite, strongly demonstrating the embedding of $Li_{0.96}Ti_{1.08}S_2$ domains in the $Li_4Ti_5O_{12}$ matrix, as illustrated in Figure 2E,F.

2.5. Ti K-Edge X-Ray Near Edge Structure (XANES)/Extended X-Ray Absorption Fine Structure (EXAFS) Analysis

The oxidation states and local symmetries of the $Li_{0.96}Ti_{1.08}S_2$–$Li_4Ti_5O_{12}$ nanocomposites are examined with Ti K-edge XANES analysis, see Figure S4 (Supporting Information). All the present

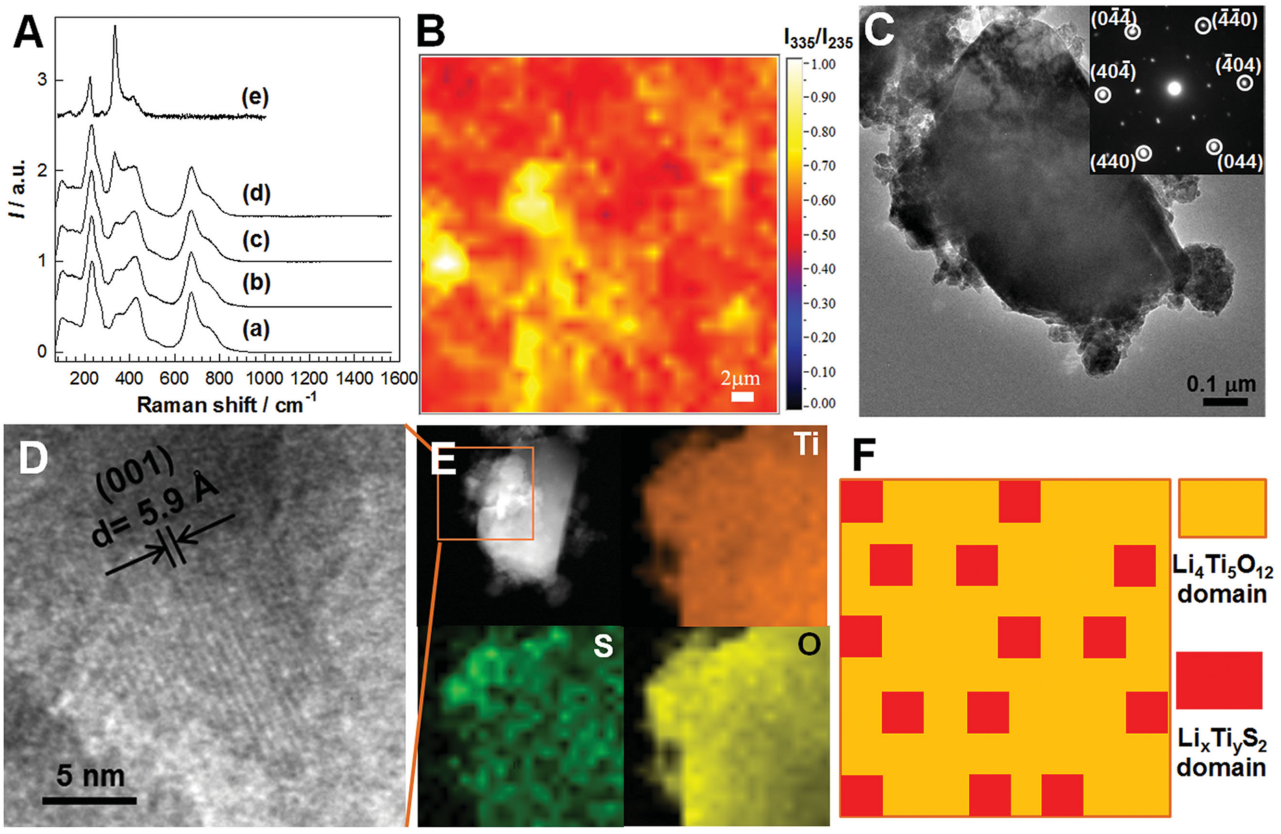

Figure 2. A) Micro-Raman spectra of (a) the pristine $Li_4Ti_5O_{12}$, the $Li_{0.96}Ti_{1.08}S_2$–$Li_4Ti_5O_{12}$ nanocomposites of b) **SLTO1**, c) **SLTO2**, and d) **SLTO3**, and e) the reference $Li_xTi_yS_2$. B) Spatial distribution of the $Li_{0.96}Ti_{1.08}S_2$ and $Li_4Ti_5O_{12}$ phases in the **SLTO3** nanocomposite from the relative Raman intensity of I_{335}/I_{235}. C) TEM image and SAED pattern, D) HR-TEM image, E) STEM-HAADF image and elemental maps of titanium, sulfur, and oxygen, and F) schematic model for the **SLTO3** nanocomposite.

nanocomposites as well as pristine $Li_4Ti_5O_{12}$ show nearly identical edge energy to the tetravalent references of anatase- and rutile-type TiO_2, confirming the tetravalent Ti^{4+} oxidation state in these materials. In the pre-edge region, all the materials under investigation exhibit weak pre-edge peaks P_1, P_2, and P_3, which are assigned as the 1s → 3d transitions.[3b–e,10] The spectral features of these peaks provide sensitive measure for the local atomic arrangement around titanium ions.[10] There is no marked difference in the shape and position of these pre-edge peaks for the pristine $Li_4Ti_5O_{12}$ and the **SLTO1**, **SLTO2**, and **SLTO3** nanocomposites, confirming the maintenance of the crystal structure of cubic spinel phase after the reaction with CS_2. In the main-edge region, several distinct peaks A, B, and C corresponding to the dipole-allowed 1s → 4p transitions are observed for all the present materials.[3b–e,10] Like the pre-edge features, these peaks in main-edge region show similar spectral features for all the nanocomposites of **SLTO1**, **SLTO2**, and **SLTO3** and the pristine $Li_4Ti_5O_{12}$, which are clearly distinguishable from the other titanium oxides. This observation provides clear evidence for the maintenance of the cubic spinel structure upon the reaction with CS_2. The $Li_xTi_yS_2$ component in the present $Li_{0.96}Ti_{1.08}S_2$–$Li_4Ti_5O_{12}$ nanocomposites is almost indiscernible with Ti K-edge XANES analysis because of its small content.

The local structural variation of titanium ion upon the reaction with CS_2 is further probed with Ti K-edge EXAFS analysis, since the EXAFS technique is more sensitive to the subtle alteration of chemical bonding nature compared with the XANES technique.[11] **Figure 3**A,B represents the experimental k^3-weighted Ti K-edge EXAFS oscillations and their Fourier transformed (FT) data of the **SLTO3** nanocomposite with the highest $Li_{0.96}Ti_{1.08}S_2$ content, the pristine $Li_4Ti_5O_{12}$, and reference $Li_xTi_yS_2$. Although the overall k^3-weighted EXAFS oscillation of **SLTO3** nanocomposite is similar to that of the pristine Li_4TiO_{12}, its EXAFS signal in high k region is closer to that of the reference $Li_xTi_yS_2$ rather than that of $Li_4Ti_5O_{12}$, reflecting the in situ formation of $Li_xTi_yS_2$ domain in the present **SLTO3** nanocomposite. Commonly for the pristine $Li_4Ti_5O_{12}$ and **SLTO3** nanocomposite, two distinct FT peaks appear at ≈1.5 and ≈2.6 Å, which are assigned as the (Ti–O) and (Ti–Ti) coordination shells. In the case of the **SLTO3** nanocomposite, additional feature is discernible at ≈2.0 Å (i.e. no phase-shift corrected distance), whose position is in good agreement with that of the (Ti–S) coordination shell of reference $Li_xTi_yS_2$. This EXAFS result provides strong evidence for the incorporation of metal sulfide domain in the $Li_4Ti_5O_{12}$ matrix after the reaction with CS_2.

2.6. X-Ray Photoelectron Spectroscopy (XPS) and Fourier Transform-Infrared (FT-IR) Analyses

The chemical bonding natures of the $Li_{0.96}Ti_{1.08}S_2$–$Li_4Ti_5O_{12}$ nanocomposites are also examined with XPS, since this

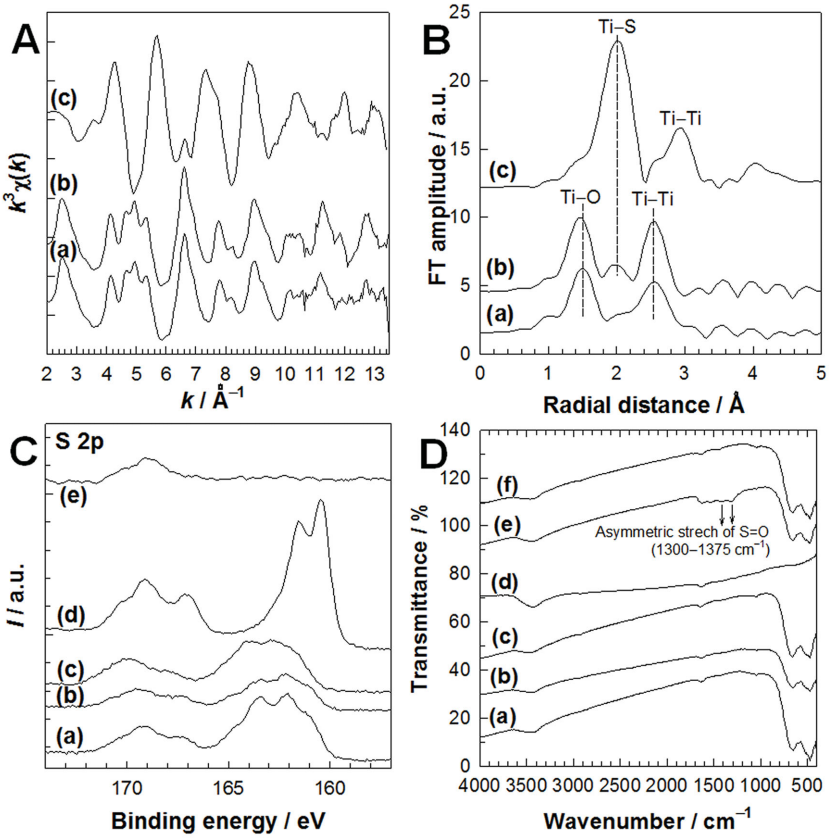

Figure 3. A) The experimental k^3-weighted EXAFS oscillations and B) FT data of Ti K-edge EXAFS spectra for a) the pristine $Li_4Ti_5O_{12}$, b) the **SLTO3** nanocomposite, and c) the reference $Li_xTi_yS_2$. C) S 2p XPS and D) FT-IR spectra of the $Li_{0.96}Ti_{1.08}S_2$–$Li_4Ti_5O_{12}$ nanocomposites of a) **SLTO1**, b) **SLTO2**, and c) **SLTO3**, d) the reference $Li_xTi_yS_2$, e) the $Li_4Ti_5O_{12}$ prepared with thiourea, and f) the pristine $Li_4Ti_5O_{12}$.

technique is quite powerful in characterizing sulfur-containing species especially formed on the surface of material. As can be seen from Figure 3C, the reference material of $Li_4Ti_5O_{12}$ prepared with thiourea displays the XPS peak centering at ≈169 eV, which corresponds to the hexavalent sulfate ion. This result is in good agreement with the previously reported S 2p XPS spectra of sulfur-doped metal oxide prepared with sulfurization agents of thiourea, ammonium sulfide, sodium sulfide, and elemental sulfur.[5] Conversely, all the present nanocomposites of **SLTO1**, **SLTO2**, and **SLTO3** demonstrate an intense but broad peak centering at ≈162.5 eV, which can be assigned as sulfide ions.[6,9d,12] In comparison with the reference $Li_xTi_yS_2$ phase showing the peak centering at ≈161 eV, the binding energy of this peak is somewhat higher for the present nanocomposites. This is attributed to the interaction of S^{2-} ions with neighboring $Li_4Ti_5O_{12}$ domains. That is, the chemical interaction between sulfide and tetravalent Ti^{4+} in $Li_4Ti_5O_{12}$ leads to the partial electron transfer from sulfur to titanium, resulting in the blue shift of the corresponding XPS feature. In addition, all the present nanocomposites as well as the reference $Li_xTi_yS_2$ display additional weak XPS peak centering at ≈169 eV, which is assigned as hexavalent sulfate ion.[5] This sulfate-related peak might originate from the minor surface species of the present materials.

The bonding state of sulfur species in the present nanocomposites is also investigated with FT-IR spectroscopy that sensitively reflects the presence of sulfur-containing species. As presented in Figure 3D, strong IR bands appear at 1300–1375 cm^{-1} in the FT-IR spectrum of the sulfur-doped $Li_4Ti_5O_{12}$ material prepared with thiourea. These spectral features correspond to asymmetric stretching vibrations of S=O, demonstrating the formation of sulfate species in the $Li_4Ti_5O_{12}$ material via the reaction with thiourea, as reported previously.[5,13] Conversely, these sulfate-related IR bands are absent in the present FT-IR spectra of all the $Li_{0.96}Ti_{1.08}S_2$–$Li_4Ti_5O_{12}$ nanocomposites, indicating the negligible concentration of the sulfate species in these materials. On the basis of the present FT-IR results, the observation of sulfate-related peak in the XPS spectra (Figure 3C) can be ascribed to the extremely high sensitivity of XPS technique to surface species. That is, the sulfate species observed from the XPS analysis exists on the surface of the nanocomposites at very low concentration.

2.7. Electrochemical Measurement

The $Li_{0.96}Ti_{1.08}S_2$–$Li_4Ti_5O_{12}$ nanocomposites of **SLTO1**, **SLTO2**, and **SLTO3** as well as the references of $Li_4Ti_5O_{12}$ and $Li_xTi_yS_2$ are tested as anode materials for LIBs to probe the influence of the introduction of conductive $Li_{0.96}Ti_{1.08}S_2$ domain on the electrochemical property of lithium titanate. As plotted in **Figure 4**A, like the pristine $Li_4Ti_5O_{12}$, all the present $Li_{0.96}Ti_{1.08}S_2$–$Li_4Ti_5O_{12}$ nanocomposites demonstrate a flat plateau of 1.55 V, strongly suggesting that the electrochemical activity of the present nanocomposites originates mainly from the $Li_4Ti_5O_{12}$ component. The reference $Li_xTi_yS_2$ is also electrochemically active with the higher working potential of 2.15 V compared with that of $Li_4Ti_5O_{12}$. But the discharge capacity of this phase is smaller than those of the other $Li_4Ti_5O_{12}$-containing materials, clearly showing its lower electrochemical activity. A high Coulombic efficiency (≈99.99%) of the pristine $Li_4Ti_5O_{12}$ material remains intact after the formation of $Li_{0.96}Ti_{1.08}S_2$ domains, indicating the high electrochemical stability of the present nanocomposites. All the present $Li_{0.96}Ti_{1.08}S_2$–$Li_4Ti_5O_{12}$ nanocomposites delivery large discharge capacities of ≈143–160 mAh g^{-1} at 1 C rate, which are much greater than those of the pristine $Li_4Ti_5O_{12}$ (≈134 mAh g^{-1}) and the reference $Li_xTi_yS_2$ (≈115 mAh g^{-1}), see Figure 4B. For comparison, we also measured the electrode performance of the physical mixture of $Li_xTi_yS_2$ and $Li_4Ti_5O_{12}$ in the molar ratio of 0.13:1, showing smaller electrode discharge capacity (≈132 mAh g^{-1}) at 1 C rate, see Figure S5 (Supporting Information). This capacity of physical mixture is notably smaller than that of **SLTO3** nanocomposite (≈160 mAh g^{-1}), underscoring the usefulness

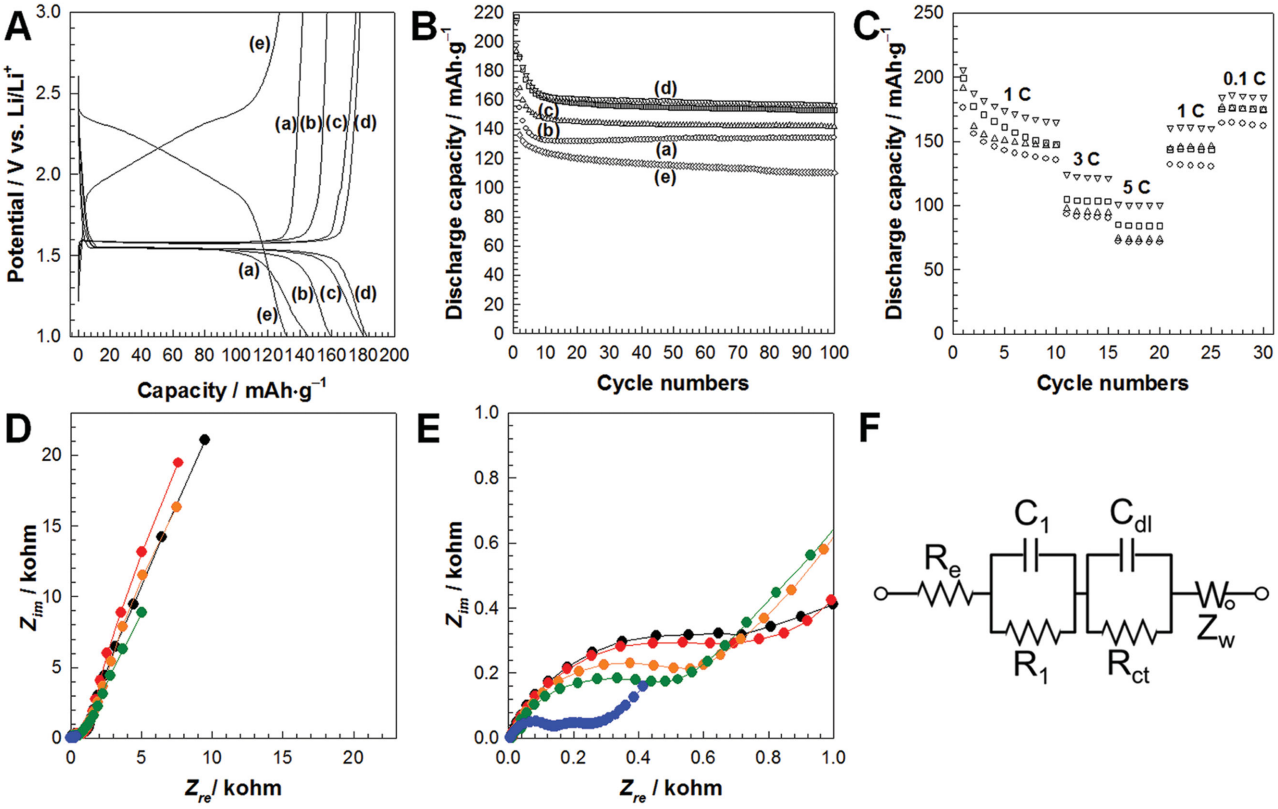

Figure 4. A) Potential profiles of the 3rd discharge–charge cycles, B) plots of discharge capacity on cycle numbers, C) C rate-dependent plots of the discharge capacity, D) Nyquist plots for the electrode/electrolyte interface, E) expanded view of Nyquist plots in the high-medium frequency region, and F) Voigt-type equivalent circuit for a) the pristine $Li_4Ti_5O_{12}$ (circles, black), the $Li_{0.96}Ti_{1.08}S_2$–$Li_4Ti_5O_{12}$ nanocomposites of b) **SLTO1** (triangles, red), c) **SLTO2** (squares, orange), and d) **SLTO3** (inverse triangles, green), and e) the reference $Li_xTi_yS_2$ (diamonds, blue).

of the embedding of $Li_xTi_yS_2$ domain in enhancing the electrochemical activity of the $Li_4Ti_5O_{12}$ material. In contrast to the $Li_{0.96}Ti_{1.08}S_2$–$Li_4Ti_5O_{12}$ nanocomposites, the sulfur-doped $Li_4Ti_5O_{12}$ prepared with thiourea delivers smaller discharge capacities (≈105 mAh g^{-1}) than those of the pristine $Li_4Ti_5O_{12}$, indicating the detrimental influence of the formation of the insulating sulfate species on the electrochemical performance of $Li_4Ti_5O_{12}$, see Figure S6 (Supporting Information). This observation underscores the usefulness of the composite formation with conductive metal sulfide in improving the electrode performance of lithium titanate. Among the present nanocomposites, the **SLTO3** material deliveries the largest discharge capacity of ≈160 mAh g^{-1} at 1 C rate, which is comparable to the best electrode performance of graphene–$Li_4Ti_5O_{12}$ nanocomposite.[3b,14] The present electrochemical measurement provides strong evidence for the usefulness of metal sulfide as a conductive additive in increasing the discharge capacity of electrode material. Although a further increase of the volume of CS_2 reactant beyond 0.6 mL induces the additional formation of the $Li_{0.96}Ti_{1.08}S_2$ phase, it has detrimental influence on the electrode performance of nanocomposite. This result is interpreted as a result of the decreased concentration of highly electrochemically active $Li_4Ti_5O_{12}$ component, see Figure S7 (Supporting Information). The beneficial effect of the composite formation with $Li_{0.96}Ti_{1.08}S_2$ is more distinct for higher current density condition, see Figure 4C. The present experimental findings clearly demonstrate that, in terms of large discharge capacity and the flatness of operating potential, the present $Li_{0.96}Ti_{1.08}S_2$–$Li_4Ti_5O_{12}$ nanocomposites are very promising as anode material for EV application.

2.8. Electrochemical Impedance Spectroscopy (EIS) Analysis

The evolution of charge-transfer behavior upon the composite formation with $Li_{0.96}Ti_{1.08}S_2$ is examined with EIS. Figure 4D illustrates the EIS spectra of the $Li_{0.96}Ti_{1.08}S_2$–$Li_4Ti_5O_{12}$ nanocomposites and the references of $Li_4Ti_5O_{12}$ and $Li_xTi_yS_2$. Among all the materials under investigation, the reference $Li_xTi_yS_2$ displays the smallest diameter of the circles, confirming much higher electrical conductivity of this metal sulfide phase compared with the other metal oxide phases. In comparison with the pristine $Li_4Ti_5O_{12}$, all of the present nanocomposites demonstrate a significant reduction in the diameter of the semicircle in the high-medium frequency region of the Nyquist plots, as can be seen clearly from Figure 4E. As the content of $Li_{0.96}Ti_{1.08}S_2$ increases, this circle becomes smaller. This observation strongly suggests the improvement of the charge-transfer kinetics of the $Li_4Ti_5O_{12}$ electrode upon the composite formation with highly conductive $Li_{0.96}Ti_{1.08}S_2$.

The modeling analysis based on the Voigt-type equivalent circuit is carried out to further analyze the evolution of charge-transfer kinetics upon the composite formation. As illustrated in Figure 4F, the R||C circuit consisting of C_1 and R_1 represents the migration of Li^+ ion through the surface film of multilayer structure, and C_{dl}, R_{ct}, and Z_w mean the double-layer capacitance, charge-transfer resistance, and Waburg impedance, respectively.[15] The slope of Z_{re} versus $\omega^{-1/2}$ plot in the Warburg region provides the Warburg coefficient σ_w, see Figure S8 (Supporting Information).[16] The validity of the present fitting analysis is evidenced by the small values of χ^2 function (χ^2 = 0.0024–0.0085). The reference $Li_xTi_yS_2$ shows the lowest values of R_{ct} (92.8 Ω) and σ_w (35.7 Ω $s^{-1/2}$), confirming its excellent conductivity. The reaction of $Li_4Ti_5O_{12}$ with CS_2 leads to the depression of R_{ct} and σ_w, indicating the improvement of the charge-transfer behavior upon the composite formation with metal conductive sulfide. Among the present nanocomposites, the **SLTO3** material with the highest $Li_{0.96}Ti_{1.08}S_2$ content displays small values of R_{ct} (255.7 Ω) and σ_w (1404.3 Ω $s^{-1/2}$), which are smaller than those of the other materials (the pristine $Li_4Ti_5O_{12}$: R_{ct} = 690.3 Ω, σ_w = 3216.0 Ω $s^{-1/2}$; **SLTO1**: R_{ct} = 655.3 Ω, σ_w = 2524.9 Ω $s^{-1/2}$; **SLTO2**: R_{ct} = 443.2 Ω, σ_w = 2340.9 Ω $s^{-1/2}$). This result clearly demonstrates the enhancement of the charge-transfer kinetics via the incorporation of conductive $Li_{0.96}Ti_{1.08}S_2$ domains. The observed improvement of charge-transfer kinetics is mainly responsible for the observed increase of the charge and discharge capacity upon the coupling with $Li_{0.96}Ti_{1.08}S_2$ species.

2.9. Application of the Present Sulfurization Method for Semiconducting Layered Titanoniobate

The universal applicability of the present method using CS_2 as a sulfurization agent is tested for the other semiconducting metal oxide of $CsTi_2NbO_7$. The detailed reaction condition is the same as that for the **SLTO2** nanocomposite (0.4 mL of liquid CS_2 for 1 g of $CsTi_2NbO_7$).[17] While the reaction with CS_2 does not cause any modification in the XRD pattern of layered $CsTi_2NbO_7$, it makes the white color of the pristine material darker, strongly suggesting the formation of conductive metal sulfide domain, see Figure S9 (Supporting Information). The preliminary cyclic voltammetry measurement demonstrates the increase of the electrochemical activity of layered titanoniobate. This result confirms the universal applicability of the present sulfurization route to improve the electrode performance of semiconducting metal oxides.

3. Conclusion

In present study, a novel synthetic strategy of the in situ formation of conductive metal sulfide domain is developed for the first time to improve the electrochemical activity of semiconducting metal oxide. The $Li_{0.96}Ti_{1.08}S_2$–$Li_4Ti_5O_{12}$ nanocomposites are synthesized by the reaction of $Li_4Ti_5O_{12}$ with CS_2 at elevated temperature. The $Li_{0.96}Ti_{1.08}S_2$ domain can be successfully embedded in the $Li_4Ti_5O_{12}$. The color change of the materials and UV–vis spectra upon the reaction with CS_2 clearly demonstrate the metallization of the semiconducting lithium titanate upon the composite formation with conductive lithium titanium sulfide. The obtained $Li_{0.96}Ti_{1.08}S_2$–$Li_4Ti_5O_{12}$ nanocomposites show very promising electrode performance, which is superior to the pristine $Li_4Ti_5O_{12}$ phase. This result underscores the advantage of the composite formation with conducting metal sulfide in enhancing the electrochemical activity of semiconducting metal oxide. The improvement of electrical connection and lithium ion diffusion path between the two components is obviously verified by the EIS measurement. The resulting enhancement of electronic and lithium ionic conductivities is mainly responsible for the excellent electrode performance of the present $Li_{0.96}Ti_{1.08}S_2$–$Li_4Ti_5O_{12}$ nanocomposites. The present experimental findings clearly demonstrate that the in situ formation of metal sulfide using CS_2 is very effective in synthesizing novel nanocomposites consisting of intimately mixed metal sulfide and metal oxide domains and also in exploring promising composite electrode materials with good rate characteristics. The universal applicability of the present method is confirmed from the improvement of the electrochemical activity of semiconducting $CsTi_2NbO_7$ upon the reaction with CS_2. The current project of our group is the application of the present method for semiconducting metal oxide–graphene nanocomposites and nanostructured semiconducting metal oxides to develop high performance electrode materials for LIBs, supercapacitors, and other emerging electricity storage devices such as Na ion and multivalent ion batteries.

4. Experimental Section

Synthesis: The pristine $Li_4Ti_5O_{12}$ was prepared by sintering the stoichiometric mixture of Li_2CO_3 and TiO_2 at 850 °C under ambient atmosphere for 36 h with intermittent grindings. The $Li_{0.96}Ti_{1.08}S_2$–$Li_4Ti_5O_{12}$ nanocomposites were in situ synthesized by the calcination of the pristine $Li_4Ti_5O_{12}$ in CS_2 flow at 450 °C for 80 min. The CS_2 flow was generated using a bubbler filled with liquid CS_2 and Ar as a carrier gas with the flow rate of 6 mL min^{-1}. To probe the effect of the concentration of metal sulfide on the electrochemical performance of $Li_4Ti_5O_{12}$, several volumes (0.2, 0.4, 0.6, and 0.8 mL) of liquid CS_2 were applied for the pristine $Li_4Ti_5O_{12}$ (1 g). The material was loaded in the quartz tube (total volume of 458 mL) without any use of a crucible. After the reaction of $Li_4Ti_5O_{12}$ with CS_2, the resulting powdery materials were washed thoroughly with hexane and acetone and subsequently dried in a convection oven at 50 °C for 12 h. As a reference, the $Li_xTi_yS_2$ material was synthesized by the soft-chemical lithiation of TiS_2 (1 g) using 1.6 M *n*-butyl lithium (0.7 mL).[7b] Additionally the other sulfur-doped $Li_4Ti_5O_{12}$ was prepared by the calcination of the pristine $Li_4Ti_5O_{12}$ (1 g) mixed with thiourea (2 g) at 400 °C for 2 h, as reported previously.[5a]

Characterization: The crystal structures of the present materials were examined with XRD. The chemical compositions of the present materials were determined with CHNS elemental analysis. Diffuse reflectance UV–vis spectra of the pristine $Li_4Ti_5O_{12}$, the $Li_{0.96}Ti_{1.08}S_2$–$Li_4Ti_5O_{12}$ nanocomposites, and the reference $Li_xTi_yS_2$ were obtained with Sinco S-4100 spectrometer using $BaSO_4$ as a reference. The crystal morphologies of the present materials were examined with FE-SEM analysis. To determine the surface area of the present materials, N_2 adsorption–desorption isotherms were measured volumetrically at 77 K after degassing of the samples at 150 °C for 3 h under vacuum. Micro-Raman spectra were recorded with a Horiba Jobin-Yvon Rabram Aramis

spectrometer. The 514.5 nm line of an Ar ion laser was used as the excitation source. The crystal shapes and local atomic arrangements of the present materials were examined with TEM/HR-TEM analysis, respectively. The elemental distributions of the present nanocomposites were examined by elemental mapping/STEM-HAADF and energy dispersive spectroscopy (EDS) analyses. Ti K-edge XANES/EXAFS analyses were carried out with the EXAFS facility installed at the beam line 10C at the Pohang Accelerator Laboratory (PAL) in Korea. XANES experiments were done at room temperature in a transmission mode using gas-ionization detectors. The energies of the Ti K-edge spectra were referenced by measuring the spectrum of Ti metal foil simultaneously. The data analysis for the experimental spectra was performed by the standard procedure reported previously.[10b,11] XPS data were recorded with a PHI 5100 Perkin-Elmer spectrometer. The chemical bonding natures of the present materials were determined with FT-IR spectroscopy.

Electrochemical Measurement: The electrode functionalities of the pristine $Li_4Ti_5O_{12}$, the $Li_{0.96}Ti_{1.08}S_2$–$Li_4Ti_5O_{12}$ nanocomposites, and the reference $Li_xTi_yS_2$ were investigated by measuring galvanostatic charge–discharge cycles. The composite electrode was prepared by mixing thoroughly the active material (80 wt%) with Super P (10 wt%) and polyvinylidene fluoride (PVDF) (10 wt%) in *N*-methyl-2-pyrrolidene and then by depositing the obtained slurry on copper foil. The active material deposited on copper foil was dried in vacuum oven at 120 °C for 12 h. The electrochemical cycling tests were carried out with the cell of Li/1 M $LiPF_6$ in ethylene carbonate (EC): diethyl carbonate (50:50 in vol%) (97 vol%) and fluoroethylene carbonate (FEC) (3 vol%)/ active material, which was assembled in a dry box. All the experiments were carried out in a galvanostatic mode with Maccor multichannel galvanostat/potentiostat in the voltage range of 1.0–3.0 V with several current densities. EIS data were measured using IVIUM impedance analyzer with the frequency range of 100 kHz to 10 mHz. Sine wave with amplitude of 10 mV at open circuit potential was applied.

Supporting Information

Supporting Information is available from the Wiley Online Library or from the author.

Acknowledgements

This work was supported by the National Research Foundation of Korea (NRF) grant funded by the Korea government (ministry of science, ICT and future planning (MSIP)) (Grant No. NRF-2014R1A2A1A10052809) and the National Research Foundation of Korea Grant funded by the Korean Government (ministry of education and science technology (MEST))" (NRF-2010-C1AAA001-2010-0029065). The experiments at PAL were supported in part by MEST and Pohang university of science and technology (POSTECH).

Received: April 13, 2015
Revised: June 3, 2015
Published online: July 6, 2015

[1] a) J.-M. Tarascon, M. Armand, *Nature* **2001**, *414*, 359; b) M. Winter, R. J. Brodd, *Chem. Rev.* **2004**, *104*, 4245; c) M. G. Kim, J. Cho, *Adv. Funct. Mater.* **2009**, *19*, 1; d) G. Jeong, Y.-U. Kim, H. Kim, Y.-J. Kim, H. J. Shon, *Energy Environ. Sci.* **2011**, *4*, 1986; e) J. B. Goodenough, K.-S. Park, *J. Am. Chem. Soc.* **2013**, *135*, 1167.

[2] a) M. Endo, C. Kim, K. Nishimura, T. Fujino, K. Miyashita, *Carbon* **2000**, *38*, 183; b) D. Aurbach, E. Zinigrad, Y. Cohen, H. Teller, *Solid State Ionics* **2002**, *148*, 405.

[3] a) T.-F. Yi, L.-J. Jiang, J. Shu, C.-B. Yue, R.-S. Zhu, H.-B. Qiao, *J. Phys. Chem. Solids* **2010**, *71*, 1236; b) S. Y. Han, I. Y. Kim, K. Y. Jo, S.-J. Hwang, *J. Phys. Chem. C* **2012**, *116*, 7269; c) S. Y. Han, I. Y. Kim, S.-J. Hwang, *J. Phys. Chem. Solids* **2012**, *73*, 1444; d) S. Y. Han, I. Y. Kim, S.-H. Lee, S.-J. Hwang, *Electrochim. Acta* **2012**, *74*, 59; e) H. Song, S.-W. Yun, H.-H. Chun, M.-G. Kim, K. Y. Chung, H. S. Kim, B.-W. Cho, Y.-T. Kim, *Energy Environ. Sci.* **2012**, *5*, 9903; f) H.-G. Jung, M. W. Jang, J. Hassoun, Y.-K. Sun, B. Scrosati, *Nat. Commun.* **2011**, *2*, 516; g) G. Du, N. Sharma, V. K. Peterson, J. A. Kimpton, D. Jia, Z. Guo, *Adv. Funct. Mater.* **2011**, *21*, 3990; h) G. J. Wang, J. Gao, L. J. Fu, N. H. Zhao, Y. P. Wu, T. Takamura, *J. Power Sources* **2007**, *174*, 1109; i) K.-S. Park, A. Benayad, D.-J. Kang, S.-G. Doo, *J. Am. Chem. Soc.* **2008**, *130*, 14930; j) Y.-Q. Wang, L. Gu, Y.-G. Guo, H. Ki, X.-Q. He, S. Tsukimoto, Y. Ikuhara, L.-J. Wan, *J. Am. Chem. Soc.* **2012**, *134*, 7874; k) J. Wang, H. Zhao, Q. Yang, T. Zhang, J. Wang, *Ionics* **2013**, *19*, 415.

[4] J. E. Huheey, E. A. Keiter, R. L. Keiter, *Inorganic Chemistry: Principles of Structure and Reactivity*, Harpercollins College Publishers, New York **1993**, pp 138–251.

[5] a) L. Zhang, C. Hu, L. Cheng, W. Ding, W. Hou, J. Chen, *Chin. J. Catal.* **2013**, *34*, 2089; b) Q. Xiang, J. Yu, M. Jaroniee, *Phys. Chem. Chem. Phys.* **2011**, *13*, 4853; c) T. Ohno, T. Mitsui, M. Matsumura, *Chem. Lett.* **2003**, *32*, 364; d) J. A. Rengifo-Herrera, E. Mielczarski, J. Mielczarski, N. C. Castillo, J. Kiwi, C. Pulgarin, *Appl. Catal. B* **2008**, *84*, 448; e) J. A. Rengifo-Herrera, K. Pierzchala, A. Sienkiewicz, L. Forró, J. Kiwi, J. E. Moser, C. Pulgarin, *J. Phys. Chem. C* **2010**, *114*, 2717; f) A. J. E. Rettie, K. C. Klavetter, J.-F Lin, A. Dolocan, H. Celio, A. Ishiekwene, H. L. Bolton, K. N. Pearson, N. T. Hahn, C. B. Mullins, *Chem. Mater.* **2014**, *26*, 1670; g) S.-H. Park, Y.-S. Lee, Y.-K. Sun, *Electrochem. Commun.* **2003**, *5*, 124; h) S. H. Park, Y.-K. Sun, K. S. Park, K. S. Nahm, Y. S. Lee, M. Yoshio, *Electrochim. Acta* **2002**, *47*, 1721.

[6] W. Jiao, N. Li, L. Wang, L. Wen, F. Li, G. Liu, H.-M. Cheng, *Chem. Commun.* **2013**, *49*, 3461.

[7] a) H. A. Hallak, P. A. Lee, *Solid State Commun.* **1983**, *47*, 503; b) A. Golub', Y. Novikov, M. Vol'pin, *Bull. Acad. Sci. (USSR), Div. Chem. Sci.* **1987**, *36*, 432.

[8] R. D. Shannon, *Acta Cryst.* **1976**, *A32*, 751.

[9] a) G.-N. Zhu, C.-X. Wang, Y.-Y. Xia, *J. Electrochem. Soc.* **2011**, *158*, A102; b) Z. Jian, L. Zhao, R. Wang, Y.-S. Hu, H. Li, W. Chen, L. Chen, *RSC Adv.* **2012**, *2*, 1751; c) C. M. Julien, *Proc. Int. Workshop "Adv. Tech. Energy Sources Invest. Test."* Bulgarian Academy of Science, Sofia **2004**, p. L2-1; d) B. R. Shin, Y. J. Nam, J. W. Kim, Y.-G. Lee, Y. S. Jung, *Sci. Rep.* **2014**, *4*, 5572.

[10] a) I. Y. Kim, J. M. Lee, T. W. Kim, H. N. Kim, H. Kim, W. Choi, S.-J. Hwang, *Small* **2012**, *8*, 1038; b) I. Y. Kim, S. Park, H. Kim, S. Park, R. S. Ruoff, S.-J. Hwang, *Adv. Funct. Mater.* **2014**, *24*, 2288.

[11] J.-H. Choy, S.-J. Hwang, N. G. Park, *J. Am. Chem. Soc.* **1997**, *119*, 1624.

[12] a) D. Gonbeau, C. Guimon, G. Pfister-Guillouzo, A. Levasseur, G. Meunier, R. Dormoy, *Surf. Sci.* **1991**, *254*, 81; b) E. L. D. Hebenstreit, W. Hebenstreit, U. Diebold, *Surf. Sci.* **2001**, *470*, 347.

[13] D. L. Pavia, G. M. Lampman, G. S. Kriz, *Introduction to Spectroscopy: A Guide for Students of Organic Chemistry*, Brooks Cole, South Melbourne, Australia, **2001**, pp. 79–80.

[14] X. Guo, H. F. Xiang, T. P. Zhou, W. H. Li, X. W. Wang, J. X. Zhou, Y. Yu, *Electrochim. Acta* **2013**, *109*, 33.

[15] M. D. Levi, D. Aurbach, *J. Phys. Chem. B* **1997**, *101*, 4630.

[16] A. Funabiki, M. Inaba, Z. Ogumi, S. Yuasa, J. Otsuji, A. Tasaka, *J. Electrochem. Soc.* **1998**, *145*, 172.

[17] K. Akatsuka, G. Takanashi, Y. Ebina, M. Haga, T. Sasaki, *J. Phys. Chem. C* **2012**, *116*, 12426.